

Very-Large-Scale Integrated High- Q Nanoantenna Pixels (VINPix)

Varun Dolia ^{1*}, Halleh Balch ¹, Sahil Dagli ¹, Sajjad Abdollahramezani ¹, Hamish Carr Delgado ¹, Parivash Moradifar ¹, Kai Chang ², Ariel Stiber ¹, Fareeha Safir ³, Mark Lawrence ^{4*}, Jack Hu ^{3*}, Jennifer Dionne ^{1*}

¹Department of Materials Science and Engineering, Stanford University, 496 Lomita Mall, Stanford, 94305, CA, USA.

²Department of Electrical Engineering, Stanford University, 350 Jane Stanford Way, Stanford, 94305, CA, USA.

³Pumpkinseed Technologies, Inc., 380 Portage Ave, Palo Alto, 94306, CA, Country.

⁴Department of Electrical & Systems Engineering, Washington University in St. Louis, 1 Brookings Drive, St. Louis, 63130, MO, USA.

*Corresponding author(s). E-mail(s): vdolia@stanford.edu; markl@wustl.edu;
jack@pumpkinseed.bio; jdionne@stanford.edu;

Abstract

Metasurfaces provide a versatile and compact approach to free-space optical manipulation and wavefront-shaping.^[1–5] Comprised of arrays of judiciously-arranged dipolar resonators, metasurfaces precisely control the amplitude, polarization, and phase of light, with applications spanning imaging,^[6–8] sensing,^[9–11] modulation,^[12–14] and computing.^[15, 16] Three crucial performance metrics of metasurfaces and their constituent resonators are the quality-factor (Q -factor), mode-volume (V_m), and ability to control far-field radiation. Often, resonators face a trade-off between these parameters: a reduction in V_m leads to an equivalent reduction in Q , albeit with more control over radiation. Here, we demonstrate that this perceived compromise is not inevitable – high- Q , subwavelength V_m , and controlled dipole-like radiation can be achieved, simultaneously. We design high- Q , very-large-scale integrated silicon nanoantenna pixels – VINPix – that combine guided mode resonance waveguides with photonic crystal cavities. With optimized nanoantennas, we achieve Q -factors exceeding 1500 with V_m less than $0.1 (\lambda/n_{\text{air}})^3$. Each nanoantenna is individually addressable by free-space light, and exhibits dipole-like scattering to the far-field. Resonator densities exceeding a million nanoantennas per cm^2 can be achieved. As a proof-of-concept application, we demonstrate spectrometer-free, spatially localized, refractive-index sensing utilizing VIN-Pix metasurfaces. Our platform provides a foundation for compact, densely multiplexed devices such as spatial light modulators, computational spectrometers, and in-situ environmental sensors.

1 Main

Photonic resonators are often evaluated by two key metrics: the quality factor (Q -factor) and the mode volume (V_m). The Q -factor of a resonator describes the degree of temporal confinement or enhancement of electromagnetic waves within the resonator, characterized by the linewidth of a mode in frequency space. On the other hand, V_m quantifies the spatial extent where electromagnetic modes are primarily concentrated. Metasurfaces – arrays of nanoscale optical resonators, stand as some of the most recent significant innovations in photonics.^[2, 9, 17–19] Owing to each resonator's ability to control the phase, amplitude, and polarization of light, metasurfaces enable precise control of far-field radiation in a compact, subwavelength-thick footprint. They promise to address the growing demand for photonic devices applicable for wearable, deployable, or point-of-care scenarios such as health and environmental monitoring,^[9, 20–24] wireless communications,^[25–27] LiDAR systems,^[28, 29] wavefront shaping,^[1, 30–36] on-chip lasing,^[37, 38] and computational spectrometry.^[39, 40] Metasurfaces have added another key metric to photonic resonators beyond Q -factor and V_m : the ability to control free-space radiation.

Mie-resonators, foundational elements of metasurfaces, confine light to deep subwavelength mode volumes and excel at manipulating light waves and controlling far-field radiation.^[2, 5, 41–44] However, such nanostructures generally display only modest Q -factors (around 10) due to their increased radiative channels. More recently, high- Q metasurfaces merging high- Q cavities with Mie antennas have emerged. These metasurfaces enable high Q -factors (>1000), controlled far-field radiation, and wavefront control, operating on the principle of free-space excitation of guided mode resonances that scatter orthogonally as a dipole.^[10, 33, 45–47] Yet, maintaining high Q -factors often requires at least one translationally invariant dimension, rendering subwavelength mode volumes a challenge. Meanwhile, high- Q photonic crystal defect cavities^[48–55] have demonstrated high Q -factors with subwavelength mode volumes, around $10^{-4}(\lambda/n)^3$, through in-plane bandgap confinements. However, they scatter light arbitrarily with limited control over free-space radiation: the free-space emission often spreads out in many directions, without a distinct or intended pattern, which leads to losses in devices. Whispering gallery resonators such as ring resonators, microtoroids, and microspheres^[56–59] achieve even higher Q -factors ranging from thousands to billions. However, these ultra-high Q -factor structures exhibit relatively large V_m values (on the order of a few to hundred cubic wavelengths). Additionally, they require fibers prism- or grating-couplers to address wave-vector mismatches due to their limited free-space coupling efficiencies. These results beg the question: can optical resonators be designed that simultaneously provide a high Q -factor, small V_m , and controlled dipolar radiation?

In this work, we present high- Q antennas that sculpt free-space light into subwavelength volumes while controlling far-field radiation with a dipole-like scattering profile. These structures merge high- Q guided mode resonance waveguides^[10, 33] with photonic crystal cavities^[48] to create free-space ultra-small mode volume, high- Q resonators. Owing to their very large-scale integration (patterned at $>1\text{M}$ antennas per cm^2 and pixelated design, we term these nanoantennas VINPix. Experimentally, we achieve Q -factors as high as ~ 4700 for individual VINPix resonators with normally incident free-space light. By incorporating a slot in our design, we predict deep subwavelength mode volumes (around $0.07(\lambda/n_{\text{air}})^3$) with experimental Q -factors surpassing 1500, showcasing heightened sensitivity to surrounding refractive index variations. As a proof of concept, we create a dense VINPix metasurface to image local refractive index variations for high-resolution and high-sensitivity spectrometer-free hyperspectral mapping.

2 The VINPix Resonator Design

Figures 1a and 1b depict the schematics of our setup and the structural design of a VINPix, respectively. Our antenna design comprises: (i) a photonic cavity section, (ii) tapered photonic mirrors sections, and (iii) padding photonic mirrors sections. Figures 1c-1f display SEM images of various antenna designs that demonstrate the variations within these sections, as will be discussed ahead. Throughout this article, all structures are based on arrays of 600 nm tall Si nanoblocks on a sapphire substrate. The first design feature of our VINPix is the cavity section. The optical cavity supports bound modes that can be coupled to normally incident free-space light as guided mode resonances by introducing a bi-periodic width perturbation, Δd , in the waveguide cavity (Supplementary Figure 1).^[33, 60–65] To achieve optical resonances in the near-infrared telecommunication frequency range, we select the average block width, d , to be 600 nm (Supplementary Figure 3). The bonding and anti-bonding guided mode resonances of interest are at 207 THz (~ 1448 nm) and 262 THz (~ 1144 nm) respectively for normally incident light with an infinitely long waveguide cavity (Figure 2a, Supplementary Figure 1). The perturbation magnitude (Δd) controls the lifetime of the guided mode resonances. Decreasing the perturbation increases the Q -factor of the modes to values as high as $\sim 240,000$ with a 10 nm perturbation (Supplementary Figure 4) for the bonding guided mode resonance (GMR) of interest. The long resonant lifetime results in a strong ~ 40 -fold increase in the electric near-field enhancement, with significant field enhancements at the nanoblocks' surface (Figure 2b). Taking into account the fabrication limitations, Δd was chosen to be 50 nm for our cavities, throughout the article, unless specified otherwise.

The second design feature of our VINPix resonator is the integration of tapered photonic mirrors. These mirrors allow us to truncate the cavity length, i.e., decrease the mode volume (V_m), while still preserving high Q -factors. Without these mirrors, the Q -factor drops by orders of magnitude due to radiation losses when we reduce the waveguide cavity length (Figure 2c). For example, the Q -factor drops from $\sim 12,000$ to 600 when the cavity length is shortened from semi-infinite to $5 \mu\text{m}$ without photonic mirrors. Notably, tapered photonic crystal mirrors have been used to confine modes within traditional one-dimensional photonic crystal cavities through band-gap effects.[66–68] Here, we employ nanoblocks of the same thickness but varying widths (d) as our individual mirror segments to create our tapered photonic mirrors section. Varying the width changes the reflection strength of a given mirror segment. The mirror strength can be calculated from a band structure calculation. Figure 2d presents a simplified band structure for a mirror segment with $d = 600 \text{ nm}$. The mode gap indicates the range of forbidden frequencies, reflected by the mirror segment. The reflection strength is contingent on the relative positions of the segment's bands and the target GMR frequency according to the formula:

$$\sqrt{\frac{(\omega_2 - \omega_1)^2}{(\omega_2 + \omega_1)^2} - \frac{(\omega_{res} - \omega_o)^2}{(\omega_o)^2}} \quad (1)$$

where ω_2 , ω_1 , and ω_0 are respectively the frequencies for the air band edge, dielectric band edge, and midgap frequency of the mirror segment, and ω_{res} is the GMR frequency.[66] By tracking the positions of the dielectric (bonding mode) and air (anti-bonding mode) bands of mirror segments with varying widths (d), we can determine their respective strengths (Supplementary Figure 2 and Figure 2e). Based on these calculations, we opted for a mirror segment with $d = 2.5 \mu\text{m}$ as the strongest mirror and a segment with $d = 600 \text{ nm}$ as our weakest mirror.

Creating a Gaussian field envelope using rationally tapered mirrors minimizes radiation losses and maximizes mode confinement in photonic crystal cavities, as demonstrated by out-of-plane Fourier analyses.[48] To achieve such a Gaussian field profile within our $15 \mu\text{m}$ -long VINPix antenna, the width of each mirror segment (d) progressively increases from the cavity end to establish a polynomial taper, adhering to the formula $X = AY^p + C$. In this expression, X symbolizes the width of the mirror segment (d), Y represents the position of the mirror segment from the end of the cavity section, p indicates the polynomial's order, and A and C are constants dictated by the minimal and maximal widths of the mirror segments in the tapered mirrors section (further details can be found in the Supplementary Information). We systematically arrange these mirror segments in an ascending order of strength within the $5 \mu\text{m}$ -long tapered mirrors sections on two ends of a $5 \mu\text{m}$ -long cavity. We examined seven distinct polynomial functions, spanning from $p = 0$ (signifying no taper or a consistent d) to $p = 6$. The mode confinement in the vertical (out-of-plane) dimension was evaluated by performing Fourier transforms of the cross-sectional electric near-field profile, to quantify the scattering within the light cone.[48, 69] Figure 2f displays a cross-sectional near-field representation of the x-component of the electric field and its corresponding Fourier transform (FT) spectrum for a VINPix resonator devoid of any perturbation ($\Delta d = 0$), with mirror sections exhibiting a zeroth-order polynomial taper. In this instance, a pronounced intensity within the radiation zone is apparent, signifying substantial radiation losses in this design. This results in a modest simulated Q -factor of approximately 1900. In stark contrast, Figure 2g showcases comparable findings for a VINPix resonator, with mirror sections illustrating a fourth-order polynomial taper. A more Gaussian-like field envelope is discerned, which correspondingly causes a marked decrease in intensity within the radiation zone and a remarkably superior Q -factor of approximately 615,000 (Supplementary Figure 5 encompasses one-dimensional line traces of the field profiles and FT spectra). Therefore, by employing rational taper functions for the mirror sections, we gain Gaussian-like field profiles inside our devices that minimize radiative losses.

3 Optimization and Measurements of High- Q VINPix Resonators

We further optimize our VINPix design with width perturbations in the cavity region, with the aim to maximize Q -factors while retaining the capability for free-space light excitation. Figure 3a illustrates simulated Q -factors for a $15 \mu\text{m}$ -long VINPix resonator with a $5 \mu\text{m}$ -long cavity, subject to varying perturbations (Δd), truncated by $5 \mu\text{m}$ -long tapered mirrors sections with different polynomial orders (p). We ascertain that a fourth-order polynomial taper yields the most optimal confinement for a vast range of perturbation magnitudes, consistent with simulations sans perturbations (Figure 2g). Employing a fourth-order polynomial taper, we conduct a coarse optimization analysis to discern optimal length ratios for various sections of the VINPix resonator. The length of the cavity section emerges as the most crucial determinant in realizing elevated Q -factors (Figure 3b). This observation is intuitive, given that the cavity section primarily facilitates coupling of free-space light into individual resonators. The taper section assumes secondary importance, dictating the count of individual mirror segments and enabling intricate tapering profiles. The padding section

is a set of strong mirrors that can be added to the end of the tapered photonic mirrors to increase confinement. We achieve calculated Q -factors, exceeding 10,000 by configuring the VINPix resonator with a cavity length of $7 \mu\text{m}$ and $4 \mu\text{m}$ -long mirror sections (Figure 3b). Figure 3c depicts the simulated normalized electric near-field intensity (log scale) at the cross-section of the optimized VINPix resonator design. The most pronounced field enhancements are discernible at the nanoblock surfaces within the cavity section. Utilizing this near-field profile, we compute the far-field response, shown in Figure 3d. Along with a near-field profile of a cross-sectional x-z monitor at the GMR wavelength (Figure 3e), our simulations culminate in a refined $15 \mu\text{m}$ -long, free-space-exitable, high- Q antenna design that produces a dipole-like far-field radiation profile with suppressed radiations to higher-orders.

We experimentally validate our VINPix resonator design using a home-built reflection microscope (detailed in Supplementary Figure 6 and Methods). Guided by insights from Figure 3b, we opt for a $7 \mu\text{m}$ -long cavity section and $4 \mu\text{m}$ -long tapered mirrors sections, without any padding sections. We fabricate and characterize individual resonators with varied polynomial orders (ranging from $p = 1$ to 6) and perturbation magnitudes ($\Delta d = 50 \text{ nm}$ and 100 nm). Figure 3f shows a scanning electron microscope (SEM) image of a representative section of an array of $15 \mu\text{m}$ -long VINPix resonators, patterned on a sapphire substrate. Illuminating the metasurface through the substrate, we employ a supercontinuum near-infrared (NIR) light source, and subsequently capture the reflected intensity using an imaging spectrometer. Figure 3g presents a spectral image obtained from five individual VINPix resonators showing that our high- Q GMRs do not rely on interdevice coupling. This makes each VINPix individually addressable enabling higher packing densities, exceeding millions per cm^2 . The characterized GMR wavelength resonates with our theoretical predictions (detailed in Supplementary Figure 7), with the manifested Fano-lineshape emerging as a byproduct of the guided mode coupling with radiative Fabry-Perot modes. Figure 3h presents Q -factors obtained from this experiment – we observe the highest confinement with a fourth-order polynomial, as anticipated from simulations. Experimentally, we achieve Q -factors peaking at roughly 4700 with $\Delta d = 50 \text{ nm}$ (and approximately 2000 with $\Delta d = 100 \text{ nm}$) for individual VINPix resonators.

4 Spatial Refractive Index Mapping on a VINPix Metasurface

We subsequently fabricated a dense VINPix metasurface to showcase potential applications in high-density, multiplexed computational spectrometry and biosensing, among others. Here, each VinPix reports the local refractive index via its spectral resonance shift, which we can record via spatially-dependent intensity variations. As illustrated in Figure 4a, we employ hyperspectral imaging to concurrently extract spectral and spatial data of individual VINPix resonators. This is achieved through a time-series of wide-field images captured on a 2D CCD array, rendering a data cube.^[9, 21] We pattern the top layer of 126 VINPix resonators with PMMA resist in the shape of an “S”. Inside the “S” is water (with refractive index ~ 1.33), while outside the “S” is PMMA resist (with refractive index ~ 1.47) as shown in Figures 4c and 4d (see Methods for details). We illuminate the metasurface with a narrow-linewidth NIR tunable laser and sweep the wavelength from 1560 nm to 1620 nm in 0.05 nm increments. Each image frame corresponds to a single illumination wavelength as schematically shown in Figure 4a and 4b. By sweeping the illumination wavelength across the resonances, we simultaneously image and collect spectra for hundreds of individually addressable resonators in a single experiment (Figure 4e).

We extract the spectral information for each resonator as schematically shown in Figures 4a and 4b. Here, R_{PMMA} is a VINPix situated outside the “S”, while R_{water} is located within the “S”. The detected resonance wavelengths at $\sim 1570 \text{ nm}$ (λ_{water}) and $\sim 1610 \text{ nm}$ (λ_{PMMA}) for the two resonator groups agree with our theoretical calculations (Supplementary Figure 8). As anticipated, the resonance wavelength for VINPix resonators enveloped by PMMA is longer, attributable to the higher effective refractive index of the encompassing medium. A spatially-resolved map of resonance shifts spanning the entire field-of-view is presented in Figure 4f. The appended histogram manifests the GMR wavelengths for all the VINPix resonators recorded in the experiment (Figure 4f).

5 Introduction of a Slot for Higher Spatial Confinement and Sensitivity

To augment the sensitivity of our imaging array, we further decrease the V_m of our VINPix resonators by incorporating a slot. Photonic crystals localize light to subwavelength mode volumes, leveraging bandgap confinements in-plane and total internal reflection out-of-plane.^[70] However, by introducing a secondary step in the light confinement strategy, slotted photonic crystal cavities have attained even smaller mode volumes on the order of $\sim 0.01 (\lambda/n_{\text{air}})^3$.^[71] Owing to electromagnetic boundary conditions, this secondary level of spatial localization mandates the field, which was formerly confined within the dielectric, to now concentrate within the air section, yet maintaining the high- Q character of the modes.^[50, 72, 73]

In order to calculate the mode volume (V_m), we utilize the conventional definition wherein V_m is determined using the electric field intensity (E) and permittivity (ϵ):

$$V_m = \frac{\int \epsilon |E|^2 dV}{\max(\epsilon |E|^2)} \quad (2)$$

By introducing a slot along the length of the VINPix, we reduce the mode volume V_m , while still maintaining relatively high Q -factors (Figure 5a, schematic, and Figure 1f, SEM image). Figure 5b compares the theoretically calculated effective V_m values for different device lengths of our waveguide cavity, VINPix design, and slotted VINPix with a 30 nm wide slot (see Supplementary Figure 9 for similar comparisons of Q -factors and Q/V_{eff}). The length ratios for the cavity, tapered mirrors, and padding mirrors sections are kept the same across all different device lengths, using the ratio that yielded the highest Q -factor in our optimizations (Figure 3b). Our VINPix resonators exhibit V_m values close to $1(\lambda/n_{\text{eff}})^3$ and as small as $\sim 0.07(\lambda/n_{\text{air}})^3$ after introducing a 30 nm wide slot. Here, n_{eff} is taken as 2.24, the average of the refractive indices of air and Si based on our waveguide cavity's design, and is used to calculate the effective V_m for both the waveguide cavity and VINPix designs. For the slotted VINPix design, the field confinement is maximum within the air slot, so $n_{\text{eff}} = n_{\text{air}} = 1$, in that case. Figure 5c illustrates the normalized cross-sectional electric field intensity of a 15 μm slotted VINPix with a 30 nm wide slot, showing an electric field enhancement of approximately 110-fold within the slot. This enhancement is significantly greater than what was observed in our infinitely long waveguide cavity (~ 40 -fold, Figure 2b) and a VINPix resonator without a slot (~ 10 -fold, Figure 3c).

In Figure 5d, we compare the experimentally measured Q -factors (circles) of the slotted VINPix with the theoretically predicted values (stars). We perform our measurements on 15 μm -long slotted VINPix resonators with $p = 4$, featuring 70 nm and 100 nm wide slots. Both simulations and experiments exhibit a decrease in the Q -factor compared to a VINPix resonator (from an average of ~ 3500 to ~ 1200) as the field is now localized within a lower refractive index medium. Nevertheless, while Q -factor decreases by $\sim 3\times$, V_m shrinks by ~ 100 -fold in simulations, boosting the effective Q/V_{eff} ratio significantly (Supplementary Figure 9). Higher Q/V_{eff} and more accessible enhanced electric fields boost the sensitivity of our slotted VINPix design. In Figure 5e, we exemplify this increased sensitivity. It is well documented that increasing NaCl concentrations increases the refractive index of water.^[74] Slotted VINPix resonators demonstrate significantly higher shifts in resonant wavelength due to a stronger field overlap in the surrounding medium. The resonator's sensing figure of merit is defined as sensitivity (resonant wavelength shift per refractive index unit or RIU change) divided by the full width at half maximum (FWHM) of the mode. We observe considerably higher resonant wavelength shifts per RIU change – 437.2 nm RIU⁻¹ with our slotted VINPix resonators – compared to 355.6 nm RIU⁻¹ without the slots. State-of-the-art affinity-based biosensors are plasmonic sensors that combine small-mode volumes with controlled dipolar radiation but generally achieve FOM values of ca. 1-10 RIU⁻¹.^[75, 76] With much higher Q -factors and subwavelength V_m , our optimized slotted VINPix design achieves an excellent FOM of ~ 440 RIU⁻¹ with effortless free-space excitation and efficiently captured controlled radiation. Notably, while ensemble sensitivity sees an averaged response manifested by the radiating field in the vicinity of the resonators, a single or few molecules adeptly placed in the slot region of high electromagnetic intensity would experience a much more pronounced interaction. This implies that, for sparse-molecule measurements in the slot region, the sensitivity enhancement is expected to be substantially greater.

6 Conclusion

In this study, we introduced densely integrated high- Q photonic nanoantennas—VINPix—that combine key features of high- Q GMR waveguide cavities and tapered photonic crystal cavities. We simultaneously achieved high Q -factors, subwavelength V_m , and controlled dipole-like radiation, with effortless free-space coupling. Utilizing rationally designed tapered photonic mirrors to truncate perturbed waveguide cavities, we experimentally showcased average Q -factors of approximately 3500 in 15 μm -long VINPix resonators. Given optimal fabrication techniques that accentuate design intricacies and mitigate flaws, our VINPix design is poised to reach Q -factors in the million range. Recognizing the burgeoning need for photonic platforms in deployable and wearable applications, we demonstrate high-resolution, high-sensitivity spatial resonance shift mapping using a spectrometer-free hyperspectral imaging setup. The introduction of a slot further refines the spatial localization in our VINPix resonator, enabling subwavelength volumes as low as $\sim 0.07(\lambda/n_{\text{air}})^3$ and heightened sensitivity to refractive index variations with an ROI of ~ 440 RIU. Notably, this sensitivity could significantly escalate, especially when analyzing isolated or few molecules – if these particles are adeptly positioned within slots where field enhancement is at its maximum. The compact footprint of our antenna imparts the potential to integrate millions of individually addressable resonators per square cm. Our work opens avenues for developing innovative integrative and/or wearable and deployable photonic platforms for

multiplexed health and environmental monitoring, enhanced vibrational spectroscopy, wavefront shaping, and on-chip spectrometry.

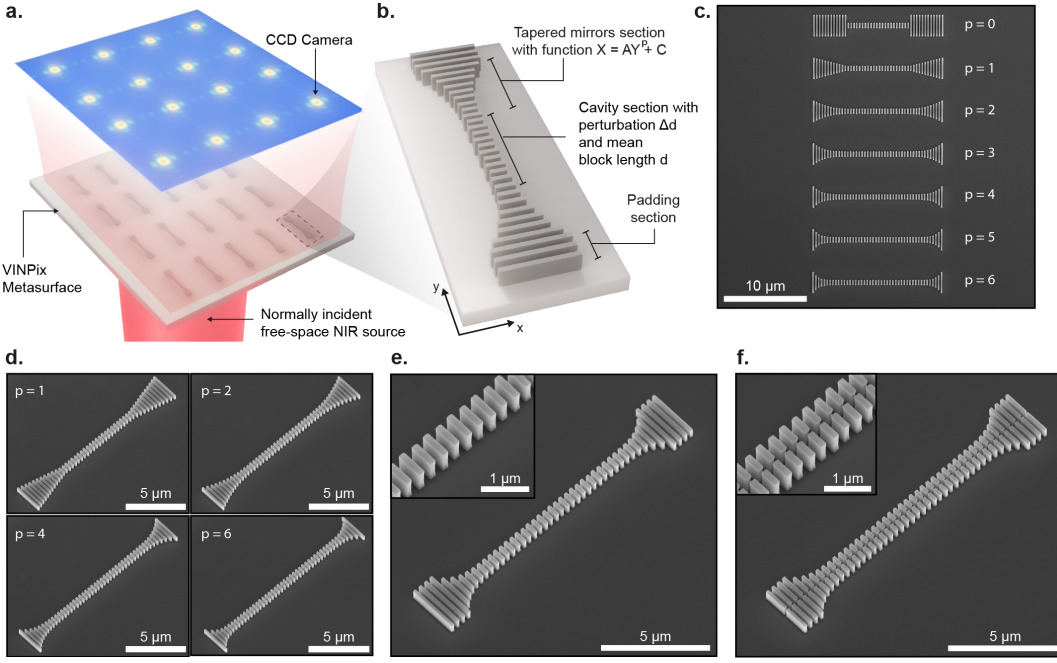


Fig. 1 Schematic and scanning electron microscopy (SEM) images of VINPix resonators: (a) Schematic of a metasurface of individually addressable $15 \mu\text{m}$ -long high- Q photonic antennas (VINPix) made of Si nanoblocks on a sapphire substrate. The resonances are excited using a normally incident near-infrared (NIR) laser source and the scattered light is recorded using a camera or an imaging spectrometer. (b) Representation of a VINPix's structural design, broken into three sections: a photonic cavity section, a tapered mirrors section, and a padding mirrors section. (c) Top view (SEM image) of VINPix resonators with different tapering functions – polynomials of order, $p = 0$ to 6 from top to bottom – without any padding sections. (d) Angled SEM images of VINPix without padding sections, and $p = 1, 2, 4$ and 6 as labeled. (e) Angled SEM image, with enlarged inset of the cavity section, of a representative $15 \mu\text{m}$ -long VINPix consisting of a $7 \mu\text{m}$ -long cavity section, $3 \mu\text{m}$ -long tapered mirrors sections and $1 \mu\text{m}$ -long padding sections. (f) Angled SEM image, with enlarged inset of the cavity section, of a slotted VINPix with a 70 nm wide slot.

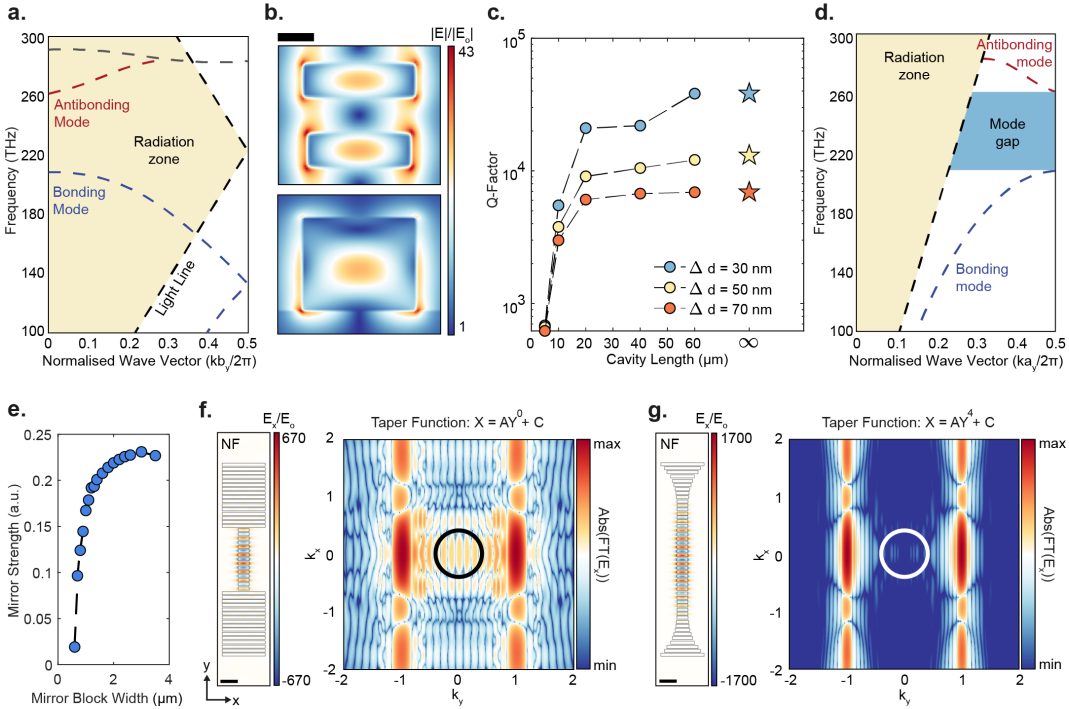


Fig. 2 Tapered photonic mirrors confine guided mode resonances to shorter resonator lengths: (a) Simplified TE band diagram of our infinitely long photonic cavity with average width, $d = 600$ nm and $\Delta d = 50$ nm, the unit cell size or periodicity (b_y) = 660 nm. Bands at 207 THz and 262 THz (for $k_{||} = 0$) are the bonding and anti-bonding guided mode resonances of interest. Refer to Supplementary Figure 1 for a schematic of our waveguide cavity and band diagram calculations (b) Simulated normalized electric field enhancements at the cross-section of the unit cell of an infinitely long cavity with $\Delta d = 50$ nm, of the bonding guided mode resonance (GMR). Geometrical parameters of the resonator unit cell are: height = 600 nm, average width (d) = 600 nm, thickness (t) = 160 nm, block spacing (a_y) = 330 nm. Scale bar 200 nm. (c) Simulated Q -factors of the GMR for waveguide cavities of different lengths. Stars correspond to waveguide cavities of infinite length (d) Simplified TE band diagram for a mirror segment with $d = 600$ nm with labeled radiation or leaky zone, light line, the bonding and anti-bonding guided mode resonances of interest, and the corresponding mode gap. Simulated mode profiles of the bonding and anti-bonding modes are shown in the Supplementary Figure 1. (e) Mirror strength calculated using band positions for mirror segments of different widths. Refer to Supplementary Figure 2 for band positions of the bonding mode (dielectric band edge), anti-bonding mode (air band edge), and the mid-gap frequency for mirror segments of different widths. (f) and (g) Left: simulated cross-sectional field profiles for the x-component of the electric field; and Right: corresponding Fourier transform spectra on a logarithmic scale to visualize the out-of-plane scattering for a VINPix with $\Delta d = 0$, with a tapered mirrors section of orders, $p = 0$ and $p = 4$, respectively. The region inside the circle is the radiation zone. Nanoblocks are marked with black borders in the cross-sectional field profiles to aid visualization. Scale bar 1 μ m.

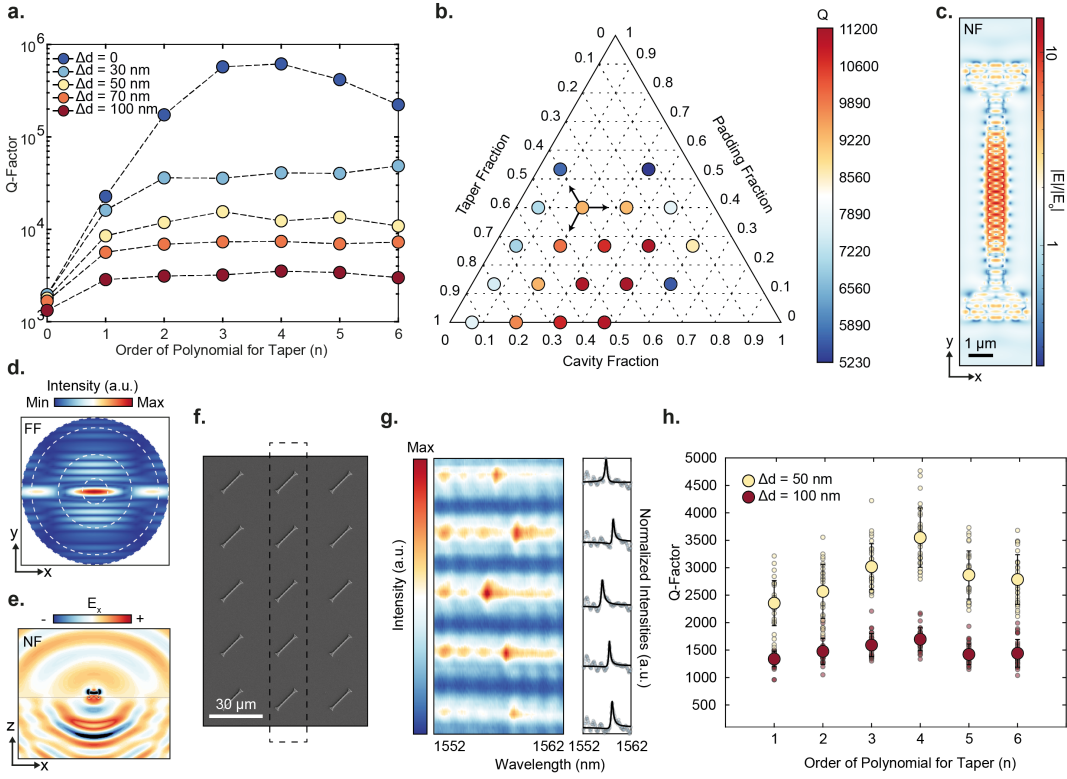


Fig. 3 Optimized VINPix resonators show dipole-like radiation and high Q-factors in experiments: (a) Simulated Q-factors of 15 μm -long VINPix with a 5 μm -long cavity of different perturbation magnitudes (Δd), and 5 μm -long tapered mirrors sections of different polynomial orders. (b) Simulated Q-factors of 15 μm -long VINPix with varying fractional configurations of the lengths of the cavity section, tapered mirrors sections ($p = 4$), and padding mirrors sections. Black arrows point towards the respective axes for one representative configuration having 0.2, 0.4 (combined, for both sides of the VINPix), and 0.4 (combined, for both sides of the VINPix) fractions of the VINPix's total length for each of the three sections respectively. (c) Simulated normalized electric near-field enhancements at the cross-section of a VINPix with 7 μm -long cavity section of $\Delta d = 50 \text{ nm}$, 3 μm -long tapered mirrors sections of $p = 4$, and 1 μm -long padding sections on each end. (d) Far-field simulation plot of the optimized VINPix. Concentric circles represent 10°, 30°, 60°, and 90° from the center respectively. (e) Simulated electric near-field profile through the cavity of the optimized VINPix. (f) Representative SEM image of an array of 15 μm -long VINPix with $p = 4$ and $\Delta d = 50 \text{ nm}$. (g) (Left panel) Spectral image from five individual VINPix as marked in (f) and (Right panel) normalized row-averaged reflected intensities corresponding to each of the five VINPix. (h) Experimentally characterized Q-factors of 15 μm -long VINPix with 7 μm -long cavity sections of $\Delta d = 50 \text{ nm}$ and 100 nm, and 4 μm -long tapered mirrors sections of different polynomial orders. Average values and standard deviations correspond to 30 VINPix resonators measured for each set.

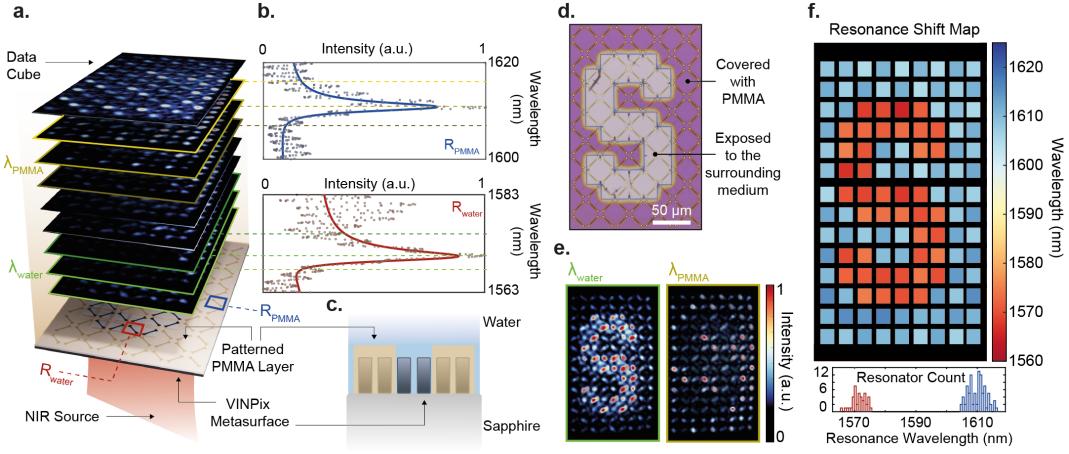


Fig. 4 VINPix metasurface successfully senses changes in the local refractive index using high-resolution hyperspectral imaging: (a) Schematic of our hyperspectral imaging setup. A VINPix metasurface patterned with a PMMA layer on top in the shape of an “S” is illuminated using a normally incident narrow band tunable NIR light source and the reflected images are recorded on a camera. (b) Extracted spectral data corresponding to R_{PMMA} and R_{water} – a VINPix resonator outside, and inside, the “S”, respectively. (c) Schematic of the PMMA patterned metasurface where certain VINPix structures are covered under PMMA. (d) Optical microscopic image of the VINPix metasurface after patterning a PMMA layer in the shape of the “S” where the resonators inside the “S” are exposed to the top medium and the rest are covered under PMMA resist. (e) Image frames recorded on the camera at the two resonance wavelengths where λ_{water} corresponds to ~ 1570 nm for GMR wavelengths of VINPix inside the “S”, and λ_{PMMA} corresponds to ~ 1610 nm for GMR wavelengths of VINPix outside the “S”. (f) (Top) Spatial resonance-shift map generated by extracting spectral information for all the 126 VINPix resonators recorded in the data cube. (Bottom) Histogram displaying the GMR wavelengths of all the recorded VINPix resonators.

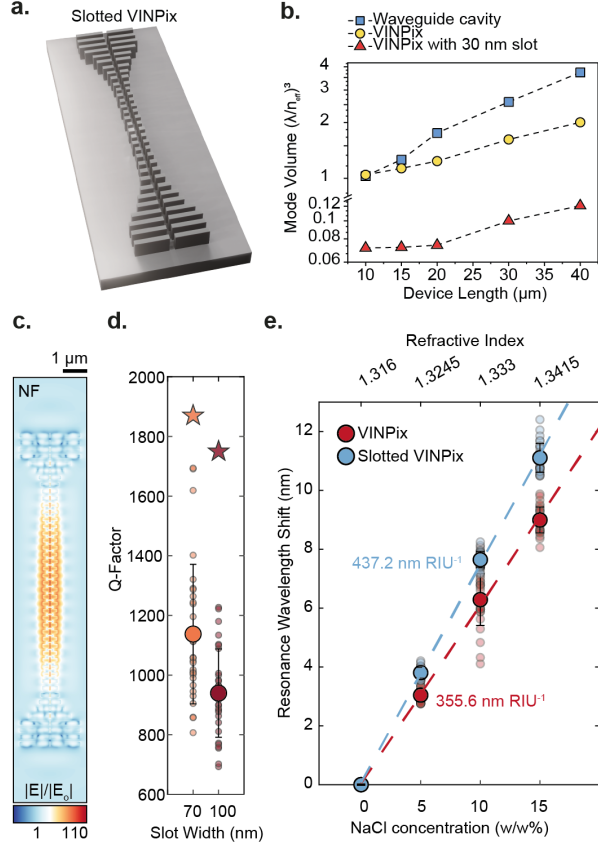


Fig. 5 Slots boost light confinement within our VINPix resonators: (a) Schematic of a slotted VINPix. (b) A comparison of simulated effective mode volumes for our perturbed waveguide cavity, optimized VINPix and a slotted VINPix with a 30 nm wide slot. (c) Simulated normalized electric field enhancements at the cross-section of a 15 μm -long slotted VINPix with a 30 nm wide slot. (d) Simulated (stars) and experimentally characterized (circles) Q -factors of slotted VINPix with 70 nm and 100 nm wide slots. Average values and standard deviations correspond to 30 slotted VINPix resonators measured for each set. (e) Resonant wavelength measurements as a function of background medium refractive index with slotted VINPix. Average values and standard deviations correspond to 30 resonators measured for each set. Lines represent linear fits to the data.

7 Methods

7.1 Computational Design

Simulations were performed using the Lumerical FDTD solver (Lumerical 2023 R1.3). PML boundary conditions in x and y directions were used for structures with finite lengths. PML boundary conditions were used in the z direction in all cases. Localized dipole sources were used to excite structures with no perturbations ($\Delta d = 0$). For structures with non-zero perturbations ($\Delta d \neq 0$), a plane wave excitation source was used in the case of periodic boundary conditions, whereas a total-field scattered-field (TFSF) excitation source was used otherwise. Consistent Q -factors were observed with all three sources for waveguide cavities of different lengths (see Supplementary Figure 11). Standalone device simulations, for example for VINPix optimizations, were performed in air as the medium. Simulations to replicate experimental results were performed in water as the medium.

7.2 Fabrication

Photonic structures were fabricated using standard lithographic procedures. First, 600 nm, single crystal silicon-on-sapphire (MTI Corporation and University Wafer) substrates were cleaned by rinsing with acetone, methanol, and isopropanol, followed by sonication in acetone and isopropanol followed by a dehydration bake at 180°C for 2 minutes. The substrates were spin-coated with hydrogen silsesquioxane (HSQ) negative tone resist (XR-1541-006, DuPont™) at 1500 RPM. The resist was baked for 5 minutes at 80°C. To reduce charging, a charge dissipation layer (e-spacer, Showa Denko) was spin-coated at 2000 RPM over the HSQ resist and baked again for 2 minutes at 80°C. The patterns were defined using electron beam lithography (Raith Voyager) with a 50 kV accelerating voltage and developed in a solution consisting of 4% sodium chloride and 1% sodium hydroxide in water. After exposure and development, the patterns were transferred to the chip using reactive ion etching (Oxford III-V Etcher) using HBr and Cl₂ chemistry for an anisotropic silicon etch. Lastly, the resist was removed using 2% hydrofluoric acid in water, followed by cleaning in a Piranha solution at 120°C to remove any organic residue. Further, for preparing VINPix metasurface for hyperspectral imaging, patterned silicon on sapphire metasurface was cleaned by rinsing with acetone, methanol, and isopropanol, followed by sonication in acetone and isopropanol followed by a dehydration bake for 2 minutes. The metasurface was spin-coated with PMMA 950A4 positive resist at 3000 RPM, followed by a 2-minute bake at 110°C. A charge dissipation layer (e-spacer, Showa Denko) was spin-coated at 2000 RPM over the HSQ resist and baked again for 2 minutes at 110°C. The PMMA patterns were defined using electron beam lithography (Raith Voyager) with a 50 kV accelerating voltage and developed in a solution consisting of a 1:3 ratio of MIBK and IPA.

7.3 Scanning Electron Microscopy Characterization

Representative images were taken using a FEI Magellan 400 XHR scanning electron microscope with a field emission gun source. A representative sample was coated with a ~ 5-nm film of Au to reduce charging. For side and tilted views, the stage was titled by 30°. Images were typically acquired with an accelerating voltage of 5 – 10 kV.

7.4 Optical Characterization

Resonator spectra were measured in a home-built near-infrared reflection microscope shown in Supplementary Figure 6. Samples were illuminated via a broadband supercontinuum laser (NKT SuperK EXTREME) or a tunable narrow-linewidth laser (SANTEC TSL-550), with a collimated fiber output. A polarizer P_1 was set to create linearly polarized incident illumination at a 45° angle with respect to the metasurface resonators. The illuminating beam is focused on the back focal plane of a 5X objective (Mitutoyo Plan Apochromat NIR) with a lens L_1 ($f = 75$ mm or $f = 100$ mm) to produce a collimated plane wave at the sample. The devices were illuminated through the sapphire substrate. To demonstrate general applicability, we characterized our VINPix metasurface under a droplet of water, following the common practice employed in biomolecular sensing. The scattered light is directed through a cross-polarized polarizer P_2 at -45° to reduce the substrate Fabry-Perot signal. The scattered light is then focused via a lens L_2 ($f = 75$ mm) into a spectrometer (Princeton Instruments SPR-2300). The broadband signal is diffracted via a diffraction grating (600 g/mm, blaze wavelength 600 nm, Princeton Instruments) and focused onto a TE cooled InGaAs CCD detector (NiRvana, Princeton Instruments). While using the Santec for hyperspectral imaging, the diffraction grating is eliminated and the images are recorded straight on the InGaAs CCD detector. Throughout the paper, the measured resonant spectral features were first normalized and then analyzed by fitting the diffraction

efficiency data with the function

$$T = \left| \frac{1}{1 + F \sin^2(n_s k h_s)} \right|^2 \cdot \left| a_r + a_i i + \frac{b}{f - f_0 + i\gamma} \right|^2 \quad (3)$$

The first term accounts for the Fabry–Perot interference through the substrate of thickness h_s and refractive index n_s . k is the free-space wavevector ($\frac{2\pi}{\lambda}$) and F accounts for the reflectivity of the interfaces. The second term represents the superposition between a constant complex background, $a_r + a_i i$, and a Lorentzian resonance with resonant frequency (f_0) and full-width at half-maximum (2γ). The Q-factor of this resonance is calculated as $Q = \frac{f_0}{2\gamma}$.

7.5 Analysis of Hyperspectral Data Cube

Each image frame in the hyperspectral data cube corresponds to a single illumination wavelength. A time series of widefield image frames representing intensity mappings were collapsed by uniform summation into a singular frame to locate VINPix centers. Pixel rows and columns corresponding to maximum intensity in the image frames were selected by determining peaks via local maxima, and manual adjustments were made based on physical VINPix spacing constraints to remove spatial overlap. VINPix centers were then assigned and labeled at each row and column cross-section. Because our VINPix size is greater than the individual pixels of our CCD camera, a 9×9 pixel intensity integration centered at our VINPix centers was performed for each frame in the hyperspectral stack. Spectral features were then extracted from each VINPix region and fitted to a Fano lineshape using the above-mentioned formula.

References

- [1] Kamali, S. M., Arbabi, E., Arbabi, A. & Faraon, A. A review of dielectric optical metasurfaces for wavefront control. *Nanophotonics* **7**, 1041–1068 (2018).
- [2] Lin, D., Fan, P., Hasman, E. & Brongersma, M. L. Dielectric gradient metasurface optical elements. *Science* **345**, 298–302 (2014).
- [3] Yu, N. & Capasso, F. Flat optics with designer metasurfaces. *Nat. Mater.* **13**, 139–150 (2014).
- [4] Yu, N. *et al.* Light propagation with phase discontinuities: generalized laws of reflection and refraction. *Science* **334**, 333–337 (2011).
- [5] Kuznetsov, A. I., Miroshnichenko, A. E., Brongersma, M. L., Kivshar, Y. S. & Luk'yanchuk, B. Optically resonant dielectric nanostructures. *Science* **354** (2016).
- [6] Huang, L. *et al.* Three-dimensional optical holography using a plasmonic metasurface. *Nat. Commun.* **4**, 1–8 (2013).
- [7] Colburn, S., Zhan, A. & Majumdar, A. Metasurface optics for full-color computational imaging. *Sci Adv* **4**, eaar2114 (2018).
- [8] Klopfer, E., Delgado, H. C., Dagli, S., Lawrence, M. & Dionne, J. A. A thermally controlled high-q metasurface lens. *Appl. Phys. Lett.* **122** (2023).
- [9] Tittl, A. *et al.* Imaging-based molecular barcoding with pixelated dielectric metasurfaces. *Science* **360**, 1105–1109 (2018).
- [10] Hu, J. *et al.* Rapid genetic screening with high quality factor metasurfaces. *Nat. Commun.* **14**, 4486 (2023).
- [11] Wu, C. *et al.* Fano-resonant asymmetric metamaterials for ultrasensitive spectroscopy and identification of molecular monolayers. *Nat. Mater.* **11**, 69–75 (2011).
- [12] Li, S.-Q. *et al.* Phase-only transmissive spatial light modulator based on tunable dielectric metasurface. *Science* **364**, 1087–1090 (2019).
- [13] Garanovich, I. L., Longhi, S., Sukhorukov, A. A. & Kivshar, Y. S. Light propagation and localization in modulated photonic lattices and waveguides. *Phys. Rep.* **518**, 1–79 (2012).
- [14] Savage, N. Digital spatial light modulators. *Nat. Photonics* **3**, 170–172 (2009).
- [15] Zangeneh-Nejad, F., Sounas, D. L., Alù, A. & Fleury, R. Analogue computing with metamaterials. *Nature Reviews Materials* **6**, 207–225 (2020).
- [16] Silva, A. *et al.* Performing mathematical operations with metamaterials. *Science* **343**, 160–163 (2014).
- [17] Arbabi, A., Horie, Y., Bagheri, M. & Faraon, A. Dielectric metasurfaces for complete control of phase and polarization with subwavelength spatial resolution and high transmission. *Nat. Nanotechnol.* **10**, 937–943 (2015).
- [18] Chen, H.-T., Taylor, A. J. & Yu, N. A review of metasurfaces: physics and applications. *Rep. Prog. Phys.* **79**, 076401 (2016).
- [19] Khorasaninejad, M. & Capasso, F. Metalenses: Versatile multifunctional photonic components. *Science* **358** (2017).
- [20] Altug, H., Oh, S.-H., Maier, S. A. & Homola, J. Advances and applications of nanophotonic biosensors. *Nat. Nanotechnol.* **17**, 5–16 (2022).
- [21] Yesilkoy, F. *et al.* Ultrasensitive hyperspectral imaging and biodetection enabled by dielectric metasurfaces. *Nat. Photonics* **13**, 390–396 (2019).

- [22] Zhang, S. *et al.* Metasurfaces for biomedical applications: imaging and sensing from a nanophotonics perspective. *Nanophotonics* **10**, 259–293 (2021).
- [23] Tseng, M. L., Jahani, Y., Leitis, A. & Altug, H. Dielectric metasurfaces enabling advanced optical biosensors. *ACS Photonics* **8**, 47–60 (2021).
- [24] Kühner, L. *et al.* Radial bound states in the continuum for polarization-invariant nanophotonics. *Nat. Commun.* **13**, 4992 (2022).
- [25] Yang, Y., Li, Q. & Qiu, M. Broadband nanophotonic wireless links and networks using on-chip integrated plasmonic antennas. *Sci. Rep.* **6**, 19490 (2016).
- [26] Cohen, M. *et al.* Wireless communication with nanoplasmonic data carriers: Macroscale propagation of nanophotonic plasmon polaritons probed by Near-Field nanoimaging. *Nano Lett.* **17**, 5181–5186 (2017).
- [27] Hu, Q. *et al.* Broadband wireless communication with space-time-varying polarization-converting metasurface. *Nanophotonics* **12**, 1327–1336 (2023).
- [28] Li, N. *et al.* A progress review on solid-state LiDAR and nanophotonics-based LiDAR sensors. *Laser Photon. Rev.* **16**, 2100511 (2022).
- [29] Li, N. *et al.* Spectral imaging and spectral LIDAR systems: moving toward compact nanophotonics-based sensing. *Nanophotonics* **10**, 1437–1467 (2021).
- [30] Klopfer, E., Dagli, S., Barton, D., 3rd, Lawrence, M. & Dionne, J. A. High-Quality-Factor Silicon-on-Lithium niobate metasurfaces for electro-optically reconfigurable wavefront shaping. *Nano Lett.* **22**, 1703–1709 (2022).
- [31] Chen, W. T., Zhu, A. Y., Sisler, J., Bharwani, Z. & Capasso, F. A broadband achromatic polarization-insensitive metalens consisting of anisotropic nanostructures. *Nat. Commun.* **10**, 355 (2019).
- [32] Wang, L. *et al.* Nonlinear wavefront control with All-Dielectric metasurfaces. *Nano Lett.* **18**, 3978–3984 (2018).
- [33] Lawrence, M. *et al.* High quality factor phase gradient metasurfaces. *Nat. Nanotechnol.* **15**, 956–961 (2020).
- [34] Yu, N. *et al.* Flat optics: Controlling wavefronts with optical antenna metasurfaces. *IEEE J. Sel. Top. Quantum Electron.* **19**, 4700423–4700423 (2013).
- [35] Jang, M. *et al.* Wavefront shaping with disorder-engineered metasurfaces. *Nat. Photonics* **12**, 84–90 (2018).
- [36] Shirmanesh, G. K., Sokhoyan, R., Wu, P. C. & Atwater, H. A. Electro-optically tunable multifunctional metasurfaces. *ACS Nano* **14**, 6912–6920 (2020).
- [37] Yang, J., Tang, M., Chen, S. & Liu, H. From past to future: on-chip laser sources for photonic integrated circuits. *Light Sci Appl* **12**, 16 (2023).
- [38] Ren, Y. *et al.* Low-threshold nanolasers based on miniaturized bound states in the continuum. *Sci Adv* **8**, eade8817 (2022).
- [39] Gao, L., Qu, Y., Wang, L. & Yu, Z. Computational spectrometers enabled by nanophotonics and deep learning. *Nanophotonics* **11**, 2507–2529 (2022).
- [40] Wang, Z. *et al.* Single-shot on-chip spectral sensors based on photonic crystal slabs. *Nat. Commun.* **10**, 1020 (2019).
- [41] Overvig, A. C. *et al.* Dielectric metasurfaces for complete and independent control of the optical amplitude and phase. *Light Sci Appl* **8**, 92 (2019).
- [42] Zheng, G. *et al.* Metasurface holograms reaching 80% efficiency. *Nat. Nanotechnol.* **10**, 308–312 (2015).

- [43] Schuller, J. A. *et al.* Plasmonics for extreme light concentration and manipulation. *Nat. Mater.* **9**, 193–204 (2010).
- [44] Kim, M.-K. *et al.* Squeezing photons into a Point-Like space. *Nano Lett.* **15**, 4102–4107 (2015).
- [45] Barton, D. *et al.* High-Q nanophotonics: sculpting wavefronts with slow light. *Nanophotonics* **10**, 83–88 (2021).
- [46] Overvig, A. C., Shrestha, S. & Yu, N. Dimerized high contrast gratings. *Nanophotonics* **7**, 1157–1168 (2018).
- [47] Kim, S., Kim, K.-H. & Cahoon, J. F. Optical bound states in the continuum with nanowire geometric superlattices. *Phys. Rev. Lett.* **122**, 187402 (2019).
- [48] Akahane, Y., Asano, T., Song, B.-S. & Noda, S. High-Q photonic nanocavity in a two-dimensional photonic crystal. *Nature* **425**, 944–947 (2003).
- [49] Hu, S. & Weiss, S. M. Design of photonic crystal cavities for extreme light concentration. *ACS Photonics* **3**, 1647–1653 (2016).
- [50] Hu, S. *et al.* Experimental realization of deep-subwavelength confinement in dielectric optical resonators. *Sci Adv* **4**, eaat2355 (2018).
- [51] Noda, S., Fujita, M. & Asano, T. Spontaneous-emission control by photonic crystals and nanocavities. *Nat. Photonics* **1**, 449–458 (2007).
- [52] Akahane, Y., Asano, T., Song, B.-S. & Noda, S. Fine-tuned high-q photonic-crystal nanocavity. *Opt. Express* **13**, 1202–1214 (2005).
- [53] Lu, X., McClung, A. & Srinivasan, K. High-Q slow light and its localization in a photonic crystal microring. *Nat. Photonics* **16**, 66–71 (2021).
- [54] Istrate, E. & Sargent, E. H. Photonic crystal heterostructures and interfaces. *Rev. Mod. Phys.* **78**, 455–481 (2006).
- [55] Joannopoulos, J. D., Johnson, S. G., Winn, J. N. & Meade, R. D. *Photonic crystals: Molding the flow of light - second edition* 2 edn (Princeton University Press, Princeton, NJ, 2008).
- [56] Matsko, A. B. & Ilchenko, V. S. Optical resonators with whispering-gallery modes-part i: basics. *IEEE J. Sel. Top. Quantum Electron.* **12**, 3–14 (2006).
- [57] Armani, D. K., Kippenberg, T. J., Spillane, S. M. & Vahala, K. J. Ultra-high-Q toroid microcavity on a chip. *Nature* **421**, 925–928 (2003).
- [58] Gorodetsky, M. L., Savchenkov, A. A. & Ilchenko, V. S. Ultimate Q of optical microsphere resonators. *Opt. Lett.* **21**, 453–455 (1996).
- [59] Lin, G., Diallo, S., Henriet, R., Jacquot, M. & Chembo, Y. K. Barium fluoride whispering-gallery-mode disk-resonator with one billion quality-factor. *Opt. Lett.* **39**, 6009–6012 (2014).
- [60] Sayanskiy, A. *et al.* Controlling high-*Q* trapped modes in polarization-insensitive all-dielectric metasurfaces. *Phys. Rev. B Condens. Matter* **99**, 085306 (2019).
- [61] Zhang, J., MacDonald, K. F. & Zheludev, N. I. Near-infrared trapped mode magnetic resonance in an all-dielectric metamaterial. *Opt. Express* **21**, 26721–26728 (2013).
- [62] Khardikov, V. V., Iarko, E. O. & Prosvirnin, S. L. A giant red shift and enhancement of the light confinement in a planar array of dielectric bars. *J. Opt.* **14**, 035103 (2012).
- [63] Lawrence, M., Barton, D. R., 3rd & Dionne, J. A. Nonreciprocal flat optics with silicon metasurfaces. *Nano Lett.* **18**, 1104–1109 (2018).
- [64] Koshelev, K., Lepeshov, S., Liu, M., Bogdanov, A. & Kivshar, Y. Asymmetric metasurfaces with High-Q resonances governed by bound states in the continuum. *Phys. Rev. Lett.* **121**, 193903 (2018).

- [65] Kupriianov, A. S. *et al.* Metasurface engineering through bound states in the continuum. *Phys. Rev. Applied* **12**, 014024 (2019).
- [66] Quan, Q., Deotare, P. B. & Loncar, M. Photonic crystal nanobeam cavity strongly coupled to the feeding waveguide. *Appl. Phys. Lett.* **96**, 203102 (2010).
- [67] Quan, Q. & Loncar, M. Deterministic design of wavelength scale, ultra-high Q photonic crystal nanobeam cavities. *Opt. Express* **19**, 18529–18542 (2011).
- [68] Zain, A. R., Johnson, N. P., Sorel, M. & De La Rue, R. M. Ultra high quality factor one dimensional photonic crystal/photonic wire micro-cavities in silicon-on-insulator (SOI). *Opt. Express* **16**, 12084–12089 (2008).
- [69] Srinivasan, K. & Painter, O. Momentum space design of high-q photonic crystal optical cavities. *Opt. Express, OE* **10**, 670–684 (2002).
- [70] Vahala, K. J. Optical microcavities. *Nature* **424**, 839–846 (2003).
- [71] Seidler, P., Lister, K., Drechsler, U., Hofrichter, J. & Stöferle, T. Slotted photonic crystal nanobeam cavity with an ultrahigh quality factor-to-mode volume ratio. *Opt. Express* **21**, 32468–32483 (2013).
- [72] Almeida, V. R., Xu, Q., Barrios, C. A. & Lipson, M. Guiding and confining light in void nanostructure. *Opt. Lett.* **29**, 1209–1211 (2004).
- [73] Choi, H., Heuck, M. & Englund, D. Self-Similar nanocavity design with ultrasmall mode volume for Single-Photon nonlinearities. *Phys. Rev. Lett.* **118**, 223605 (2017).
- [74] Saunders, J. E., Sanders, C., Chen, H. & Loock, H.-P. Refractive indices of common solvents and solutions at 1550 nm. *Appl. Opt.* **55**, 947–953 (2016).
- [75] Hao, F. *et al.* Symmetry breaking in plasmonic nanocavities: subradiant LSPR sensing and a tunable fano resonance. *Nano Lett.* **8**, 3983–3988 (2008).
- [76] Anker, J. N. *et al.* Biosensing with plasmonic nanosensors. *Nat. Mater.* **7**, 442–453 (2008).

Supplementary Information: Very-Large-Scale Integrated High- Q Nanoantenna Pixels (VINPix)

Varun Dolia ^{1*}, Halleh Balch ¹, Sahil Dagli ¹, Sajjad Abdollahramezani ¹, Hamish Carr Delgado ¹, Parivash Moradifar ¹, Kai Chang ², Ariel Stiber ¹, Fareeha Safir ³, Mark Lawrence ^{4*}, Jack Hu ^{3*}, Jennifer Dionne ^{1*}

¹Department of Materials Science and Engineering, Stanford University, 496 Lomita Mall, Stanford, 94305, CA, USA.

²Department of Electrical Engineering, Stanford University, 350 Jane Stanford Way, Stanford, 94305, CA, USA.

³Pumpkinseed Technologies, Inc., 380 Portage Ave, Palo Alto, 94306, CA, Country.

⁴Department of Electrical & Systems Engineering, Washington University in St. Louis, 1 Brookings Drive, St. Louis, 63130, MO, USA.

*Corresponding author(s). E-mail(s): vdolia@stanford.edu; markl@wustl.edu; jack@pumpkinseed.bio; jdionne@stanford.edu;

Abstract

Metasurfaces provide a versatile and compact approach to free-space optical manipulation and wavefront-shaping.^[1–5] Comprised of arrays of judiciously-arranged dipolar resonators, metasurfaces precisely control the amplitude, polarization, and phase of light, with applications spanning imaging,^[6–8] sensing,^[9–11] modulation,^[12–14] and computing.^[15, 16] Three crucial performance metrics of metasurfaces and their constituent resonators are the quality-factor (Q -factor), mode-volume (V_m), and ability to control far-field radiation. Often, resonators face a trade-off between these parameters: a reduction in V_m leads to an equivalent reduction in Q , albeit with more control over radiation. Here, we demonstrate that this perceived compromise is not inevitable – high- Q , subwavelength V_m , and controlled dipole-like radiation can be achieved, simultaneously. We design high- Q , very-large-scale integrated silicon nanoantenna pixels – VINPix – that combine guided mode resonance waveguides with photonic crystal cavities. With optimized nanoantennas, we achieve Q -factors exceeding 1500 with V_m less than $0.1 (\lambda/n_{\text{air}})^3$. Each nanoantenna is individually addressable by free-space light, and exhibits dipole-like scattering to the far-field. Resonator densities exceeding a million nanoantennas per cm^2 can be achieved. As a proof-of-concept application, we demonstrate spectrometer-free, spatially localized, refractive-index sensing utilizing VINPix metasurfaces. Our platform provides a foundation for compact, densely multiplexed devices such as spatial light modulators, computational spectrometers, and in-situ environmental sensors.

1 Supplementary note 1: High-*Q* GMR waveguide cavity design

Supplementary Figure 1a schematically shows our High-*Q* GMR waveguide cavity design. As explained in the main text, our waveguide cavity supports bound guided modes which are coupled to free-space light as guided mode resonances (GMRs) after introducing bi-periodic perturbations in our cavity design. The bi-periodic perturbation is introduced by altering the width of every other nanoblock. This symmetry breaking overcomes the wavevector mismatch and enables free space light to couple, in this case, at normal incidence. Note that the unit cell size in the *y*-direction would be twice in case of the perturbed waveguide cavity as compared to the unperturbed waveguide cavity. This changes the Bloch condition on the dispersion, folding the bands when the perturbation is introduced. Dispersion diagrams in Figure 2d and Supplementary Figure 1b correspond to a waveguide cavity without any perturbation, whereas Figure 2a corresponds to waveguide cavity with a bi-periodic width perturbation (of $\Delta d = 50$ nm).

Supplementary Figure 1c shows the cross-sectional E_x field profiles of the bonding and the anti-bonding guided modes of interest, excited using localized dipole sources. As mentioned in the main text, the resonance wavelengths of our GMRs can be easily altered by changing the dimensions of our constituent nanoblocks. In Supplementary Figure 3, we show the resonances for three different cavities with average block widths of 500, 600, and 700 nm. Lastly, the magnitude of perturbation introduced (Δd) controls the lifetime of modes, as well as the coupling efficiency of the free-space light. Decreasing the perturbation magnitude significantly increases the *Q*-factors as shown with simulations in Supplementary Figure 4. Dimensions of the nanoblocks used in our waveguide cavities are schematically shown in Supplementary Figure 1b (right): the width (d) = 600 nm, thickness (t) = 160 nm, height (h) = 600 nm, interblock spacing along the *y*-direction (a_y) = 330 nm.

2 Supplementary note 2: Designing tapered photonic mirrors

As schematically shown in Figure 1b, our mirror sections consist of nanoblocks that have similar thicknesses (t) but varying widths (d) as compared to the nanoblocks in the waveguide cavity section. The interblock spacing (a_y) is maintained constant throughout the antenna to minimize additional losses caused by any potential phase mismatch. As mentioned in the main text, the mirror strength can be calculated from the mirror segment's bands and the target GMR frequency using the formula:

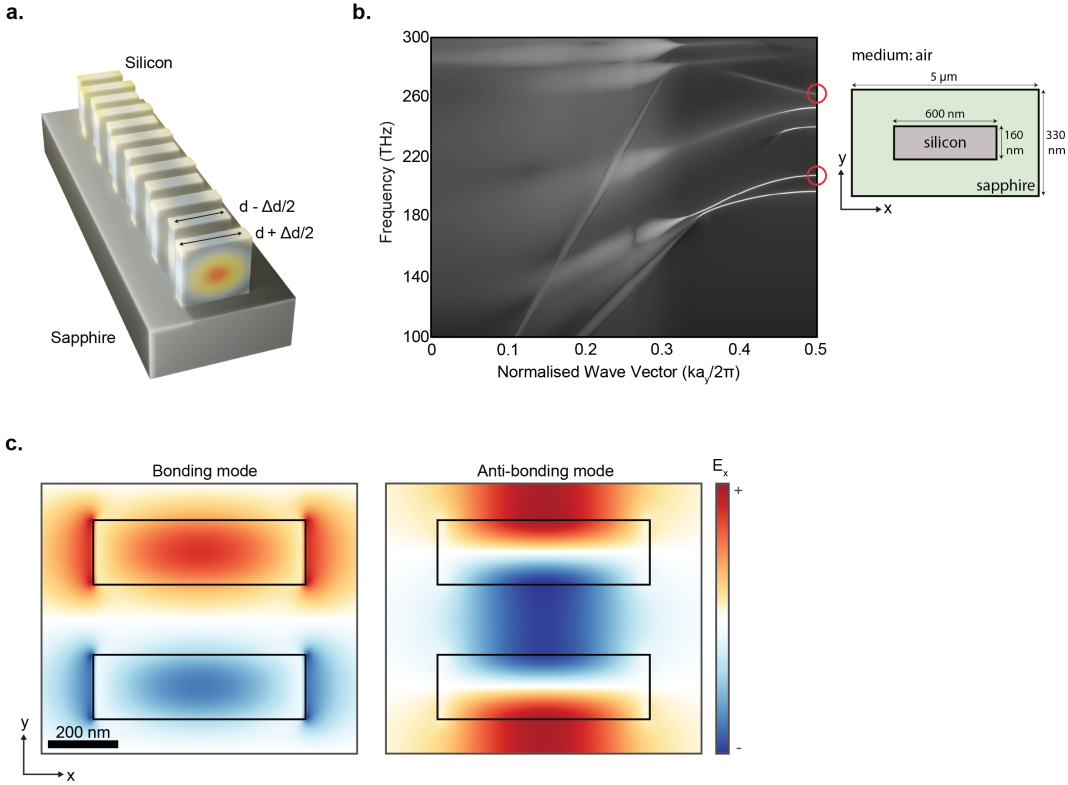
$$\sqrt{\frac{(\omega_2 - \omega_1)^2}{(\omega_2 + \omega_1)^2} - \frac{(\omega_{res} - \omega_o)^2}{(\omega_o)^2}} \quad (1)$$

where ω_2 , ω_1 , and ω_0 are respectively the frequencies for the air band edge, dielectric band edge, and midgap frequency of the mirror segment, and ω_{res} is the GMR frequency.[17]

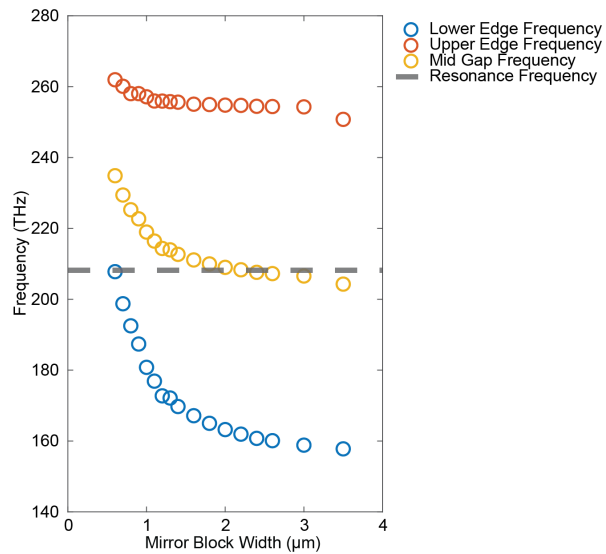
To get the highest confinement, it is imperative to have a Gaussian-like enveloping field profile within our devices, as shown by out-of-plane Fourier analyses.[18] To achieve this, we arrange mirror segments in order of increasing strengths within 5 – μm -long tapered mirrors sections on two ends of a 5 – μm -long cavity. We increase the width of each mirror segment (d) from the cavity end to establish a polynomial taper, following the form $X = AY^p + C$. Here, X represents the width of the mirror segment (d), Y denotes the position of the mirror segment from the cavity section's end, "p" signifies the order of the polynomial, and A and C are constants determined by the minimum and maximum widths of the mirror segments in the tapered mirrors section. The width of every mirror segment is decided using the following equation based on the tapering polynomial order (p) chosen:

$$X = \frac{(d_{\max} - d_{\min})}{N_{\text{taper}} - 1} Y^p + d_{\min} \quad (2)$$

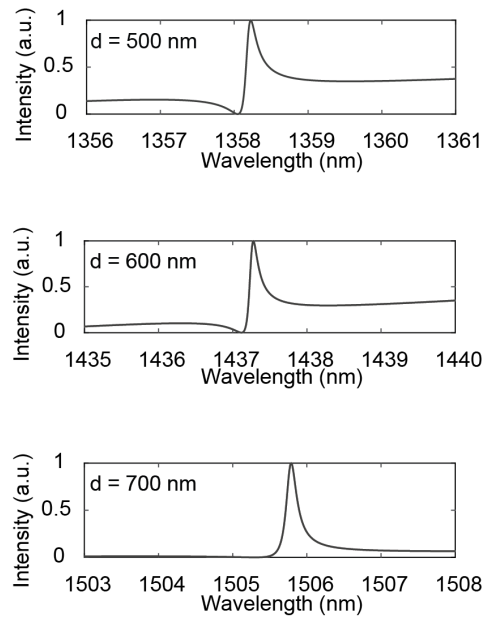
Where, X is the width of the mirror segment, d_{\max} and d_{\min} are the maximum and minimum block widths corresponding to the strongest and the weakest mirrors, which are arranged at the end and the beginning of the tapered mirrors sections from the cavity's end, respectively. N_{taper} is the total number of mirror segments within the tapered mirrors section and Y is the number/position of the particular mirror segment within the tapered mirrors section with the weakest mirror (first) being at the 0th position and the strongest mirror (last) being at the $(N_{\text{taper}} - 1)$ th position. Seven different polynomial functions, ranging from $p = 0$ (representing no taper or a constant d) to $p = 6$ were tested.



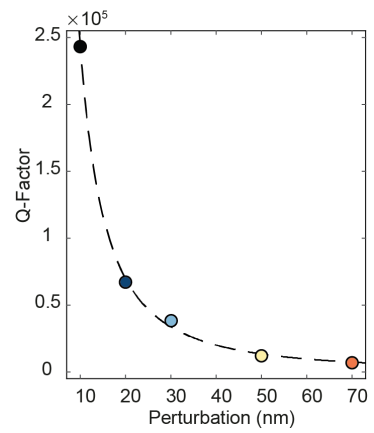
Supplementary Figure 1 (a) Rendered schematic of the waveguide cavity design with alternate sections of silicon and air. Alternate Si blocks are perturbed by Δd , with an average width of d . (b) Simulated band structure calculation of a Si block with $d = 600$ nm. The bonding and anti-bonding modes are marked with red circles at 207 THz and 262 THz respectively. Right schematic indicates the rest of the dimensions (figure not drawn to scale). (c) Cross-sectional E_x field profiles of the bonding and anti-bonding guided modes of interest in an infinitely long waveguide cavity with $d = 600$ nm and $\Delta d = 0$ nm.



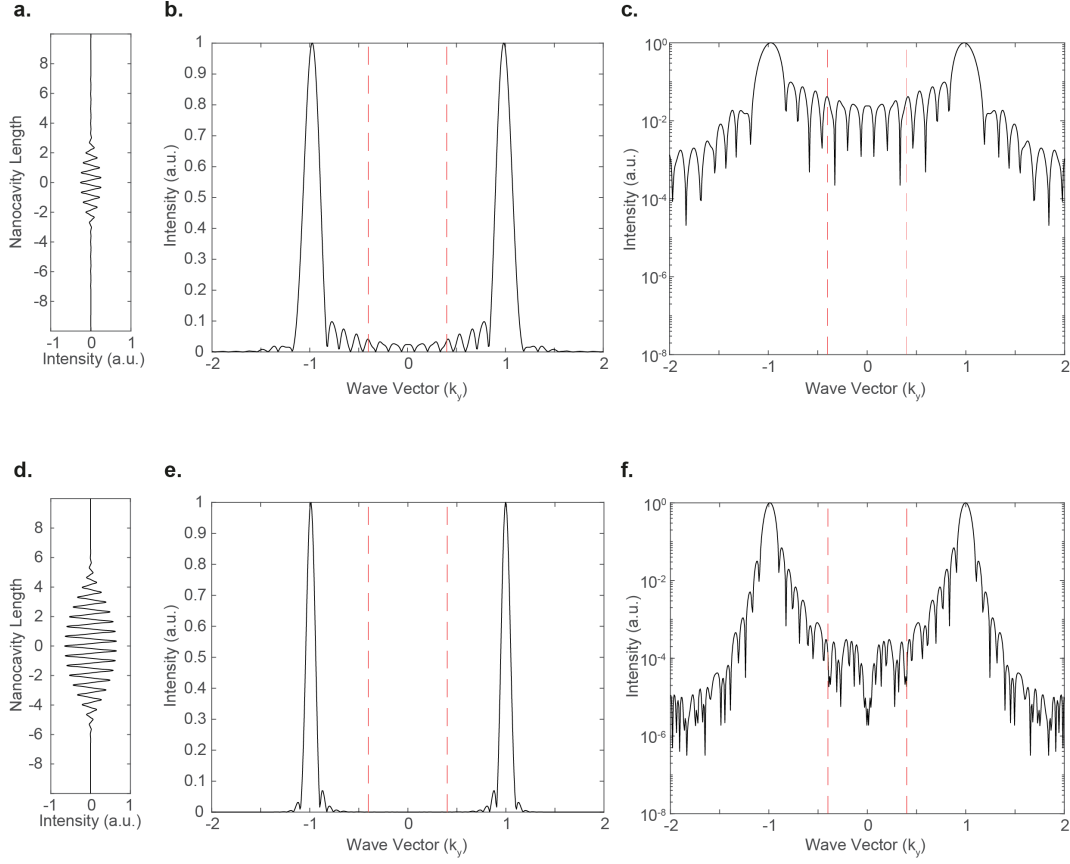
Supplementary Figure 2 Band positions of the bonding (lower-edge), anti-bonding (upper-edge), the calculated mid-gap frequency, and the target resonance frequency for Si mirror segments of different widths.



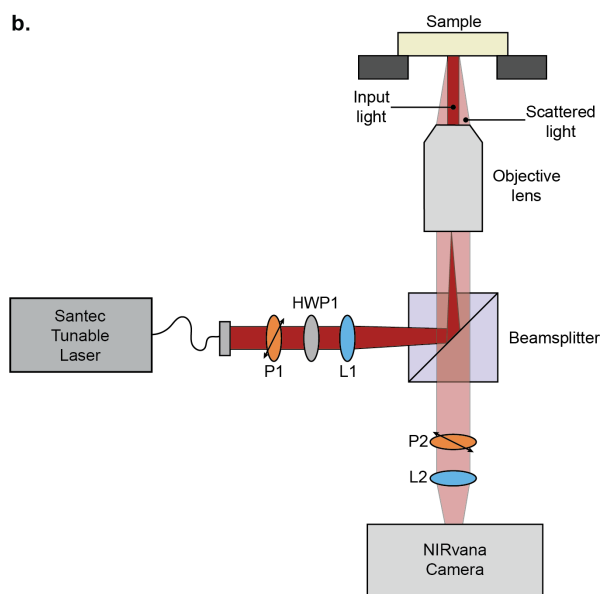
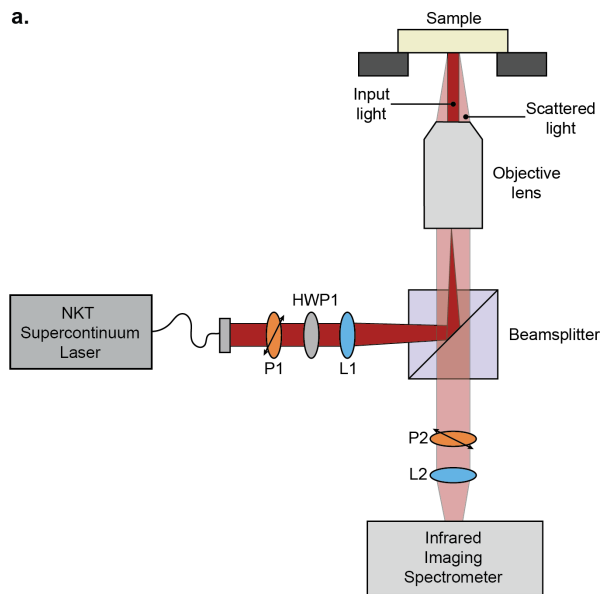
Supplementary Figure 3 Simulated normalized reflection intensities of guided mode resonances of infinitely long waveguide cavities with different average block widths d . Resonance frequencies can be easily tuned in the near-IR based on the application in hand.



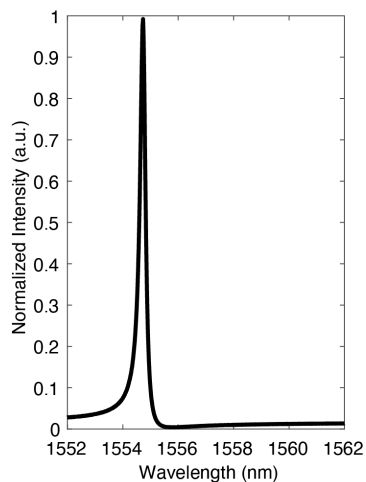
Supplementary Figure 4 Simulated Q-factors of the GMR with different perturbation magnitudes Δd for an infinitely long waveguide cavity.



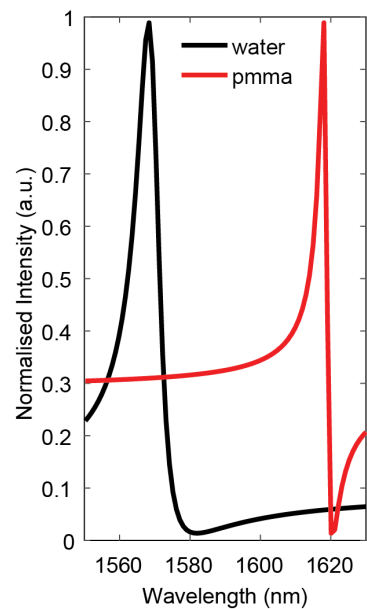
Supplementary Figure 5 Top panel corresponds to a $15\ \mu\text{m}$ -long VINPix antenna with $5\ \mu\text{m}$ cavity section and $5\ \mu\text{m}$ -long tapered mirrors section with a constant taper $p = 0$. Bottom panel corresponds to the same with a fourth-order polynomial taper $p = 4$. (a) and (d) are line-cuts of the cross-sectional E_x field profiles along corresponding to Figure 2f and 2g, along the centre of the VINPix antenna. (b) and (e) are line cuts of absolute Fourier transforms of the field profiles along $k_x = 0$. (c) and (f) are the Fourier transforms represented on a logarithmic scale. Region between the two red dashed lines in each plot is the light cone.



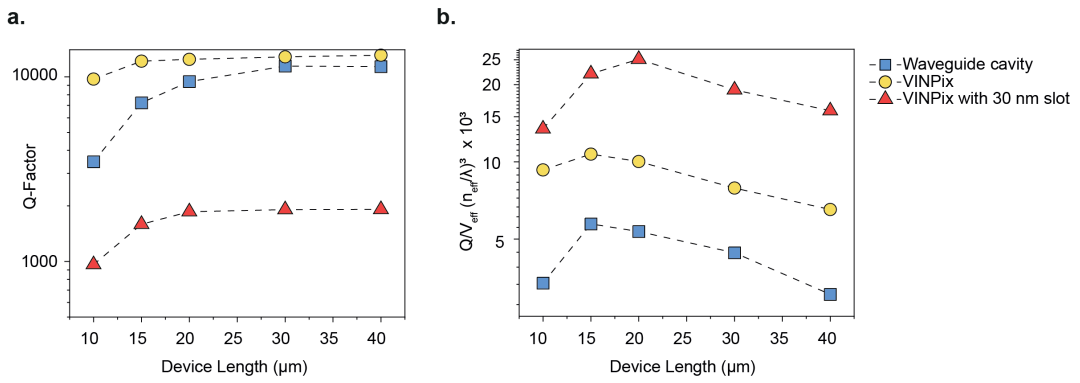
Supplementary Figure 6 Schematic of near-IR microscope setup used for collecting spectra from metasurfaces in reflection, using (a) a supercontinuum laser source and imaging spectrometer, and (b) a tunable laser source with an IR camera, for spectrometer-free hyperspectral imaging.



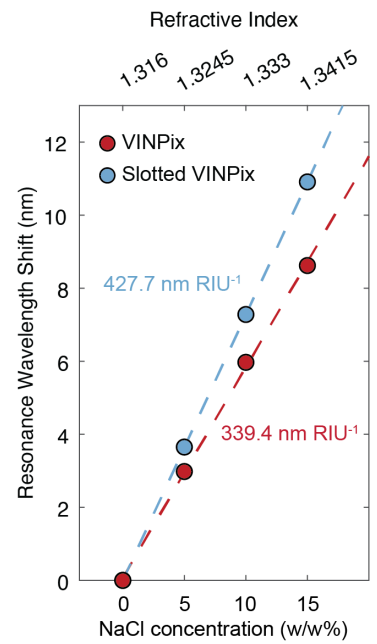
Supplementary Figure 7 Simulated reflection spectrum of 15 μm -long optimized VINPix in water to compare resonance wavelengths in experiments.



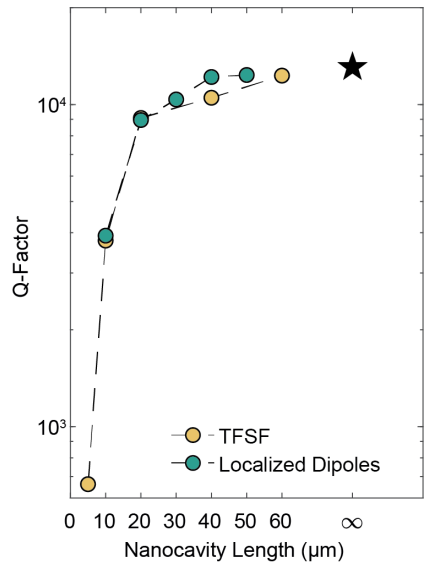
Supplementary Figure 8 Simulated reflection spectrum of $20\ \mu\text{m}$ -long VINPix. First simulation (black) corresponds to a VINPix resonator submerged in water. Second simulation (red) corresponds to a VINPix resonator covered with PMMA resist and submerged in water. These simulations were performed to roughly replicate resonance wavelengths in the hyperspectral imaging experiment (Figure 4 of main text).



Supplementary Figure 9 Comparison of simulated (a) Q -factors and (b) Q/V_{eff} for our perturbed waveguide cavity, optimized VINPix, and a slotted VINPix with a 30 nm wide slot.



Supplementary Figure 10 Simulated shifts in resonant wavelength as a function of background medium refractive index to compare with experimental measurements in Figure 5e.



Supplementary Figure 11 Comparison of simulated Q-factors on exciting waveguide cavities with different sources.

References

- [1] Kamali, S. M., Arbabi, E., Arbabi, A. & Faraon, A. A review of dielectric optical metasurfaces for wavefront control. *Nanophotonics* **7**, 1041–1068 (2018).
- [2] Lin, D., Fan, P., Hasman, E. & Brongersma, M. L. Dielectric gradient metasurface optical elements. *Science* **345**, 298–302 (2014).
- [3] Yu, N. & Capasso, F. Flat optics with designer metasurfaces. *Nat. Mater.* **13**, 139–150 (2014).
- [4] Yu, N. *et al.* Light propagation with phase discontinuities: generalized laws of reflection and refraction. *Science* **334**, 333–337 (2011).
- [5] Kuznetsov, A. I., Miroshnichenko, A. E., Brongersma, M. L., Kivshar, Y. S. & Luk'yanchuk, B. Optically resonant dielectric nanostructures. *Science* **354** (2016).
- [6] Huang, L. *et al.* Three-dimensional optical holography using a plasmonic metasurface. *Nat. Commun.* **4**, 1–8 (2013).
- [7] Colburn, S., Zhan, A. & Majumdar, A. Metasurface optics for full-color computational imaging. *Sci Adv* **4**, eaar2114 (2018).
- [8] Klopfer, E., Delgado, H. C., Dagli, S., Lawrence, M. & Dionne, J. A. A thermally controlled high-q metasurface lens. *Appl. Phys. Lett.* **122** (2023).
- [9] Tittl, A. *et al.* Imaging-based molecular barcoding with pixelated dielectric metasurfaces. *Science* **360**, 1105–1109 (2018).
- [10] Hu, J. *et al.* Rapid genetic screening with high quality factor metasurfaces. *Nat. Commun.* **14**, 4486 (2023).
- [11] Wu, C. *et al.* Fano-resonant asymmetric metamaterials for ultrasensitive spectroscopy and identification of molecular monolayers. *Nat. Mater.* **11**, 69–75 (2011).
- [12] Li, S.-Q. *et al.* Phase-only transmissive spatial light modulator based on tunable dielectric metasurface. *Science* **364**, 1087–1090 (2019).
- [13] Garanovich, I. L., Longhi, S., Sukhorukov, A. A. & Kivshar, Y. S. Light propagation and localization in modulated photonic lattices and waveguides. *Phys. Rep.* **518**, 1–79 (2012).
- [14] Savage, N. Digital spatial light modulators. *Nat. Photonics* **3**, 170–172 (2009).
- [15] Zangeneh-Nejad, F., Sounas, D. L., Alù, A. & Fleury, R. Analogue computing with metamaterials. *Nature Reviews Materials* **6**, 207–225 (2020).
- [16] Silva, A. *et al.* Performing mathematical operations with metamaterials. *Science* **343**, 160–163 (2014).
- [17] Quan, Q., Deotare, P. B. & Loncar, M. Photonic crystal nanobeam cavity strongly coupled to the feeding waveguide. *Appl. Phys. Lett.* **96**, 203102 (2010).
- [18] Akahane, Y., Asano, T., Song, B.-S. & Noda, S. High-Q photonic nanocavity in a two-dimensional photonic crystal. *Nature* **425**, 944–947 (2003).